Comptes Rendus

Chimie

Faten Eshrati Yeganeh, Mohammad Yousefi, Malak Hekmati
and Maryam Bikhof

Photocatalytic degradation of coomassie blue G-250 by magnetic NiFe$_2$O$_4$/ZnO nanocomposite

Full paper / *Mémoire*

Photocatalytic degradation of coomassie blue G-250 by magnetic NiFe$_2$O$_4$/ZnO nanocomposite

Faten Eshrati Yeganeh [a]**, Mohammad Yousefi**[*, b]**, Malak Hekmati** [c] **and Maryam Bikhof** [d]

[a] Department of Chemistry, Science and Research Branch, Islamic Azad University, Tehran, Iran

[b] Department of Chemistry, Yadegar-e Imam Khomeini (RAH) Shahr-e Rey Branch, Islamic Azad University, Tehran, Iran

[c] Department of Organic Chemistry, Faculty of Pharmaceutical Chemistry, Tehran Medical Sciences, Islamic Azad University, Tehran, Iran

[d] Department of Biology, Yadegar-e Imam Khomeini (RAH) Shahr-e Rey Branch, Islamic Azad University, Tehran, Iran

E-mails: ffyeganeh@gmail.com (F. Eshrati Yeganeh), myousefi50@hotmail.com (M. Yousefi), dr.m.hekmati@gmail.com (M. Hekmati), Maryam.bikhof@gmail.com (M. Bikhof)

Abstract. Photocatalysts NiFe$_2$O$_4$, ZnO, and NiFe$_2$O$_4$/ZnO were successfully synthesized and characterized by Fourier transform infrared spectroscopy, X-ray diffraction, scanning electron microscopy, and vibrating sample magnetometry techniques. The prepared photocatalysts demonstrated significant photocatalytic efficiency under visible and UV light. The rate of dye degradation of NiFe$_2$O$_4$/ZnO in both UV and visible ranges exceeded that of ZnO and NiFe$_2$O$_4$. Moreover, NiFe$_2$O$_4$/ZnO exhibited the most excellent photocatalytic efficiency toward Coomassie blue G-250. The effect of pH on the dye degradation rate was also monitored. Accordingly, 96.90% and 68.55% dye degradation efficiencies were achieved by NiFe$_2$O$_4$/ZnO in 30 min under UV and visible light, respectively.

Keywords. NiFe$_2$O$_4$/ZnO nanocomposites, Photocatalyst, pH value, Visible light, UV light, Coomassie blue G-250.

1. Introduction

Recently, water pollution has become a very serious problem, which has increased due to scientific progress and the rapid growth of industry. It has been estimated that approximately 40,000 tons of dyes end up in wastewater streams. The rapid industrial growth has caused environmental pollution (in particular, water contamination) due to the release of toxic compounds such as textile dyes, rubber, plastic, aromatic materials, and paper, which can cause irreparable damage to human cells, leading to diseases such as cancer [1–4]. The presence of dyes and pigments in water resources has created significant problems that cannot be resolved appro-

---

* Corresponding author.

priately by conventional water treatments. Therefore, a practical method should be developed to eliminate dye-contaminated textile effluents. Studies on chlorine-disinfected waters have indicated that disinfection byproducts are produced as a result of the reaction of chlorine with the matter present in water. Various methods, such as active carbon adsorption, ion exchange, electrolysis filtration, biodegradation, and catalysis, have been employed to remove these contaminants [5–7]. Among the various separation methods, oxidation processes, especially photocatalysis, have exhibited superiority over conventional filtration processes [8,9].

Semiconductors are used in photocatalytic oxidation for an optimal combination of proper electronic structure, light absorption properties, and the lifetime of the excited state. In general, the photocatalytic process in semiconductors relies on the migration of electrons and holes to the surface [10–12]. This migration leads to the degradation of adsorbed pollutants through their reduction or oxidation [13]. Among the studied semiconductors, ZnO has been widely employed for UV-range photocatalysis due to its proper photocatalytic activity, surface properties, and facile preparation [14]. Some researchers have reported the superiority of ZnO photocatalysts over other quantum dots due to their higher quantum efficiency, non-toxicity, chemical stability, and lower cost [15–18]. Unfortunately, the wide bandgap of ZnO is not suitable for sunlight absorption. Numerous attempts have been made to tune its bandgap from the UV to the visible range through the use of metals, non-metals, and metal oxides to improve the ZnO performance [19,20]. Owing to its cubic structure, magnetic saturation, and narrow bandgap, nickel ferrite is an important spinel ferrite suitable for this purpose. A combination of ZnO quantum dot and nickel ferrite was configured as a semiconductor photocatalyst with enhanced activity under visible light [21]. Moreover, the presence of nickel ferrite facilitates photocatalysis in water as it can be easily separated by applying an external magnetic field [18,22–25].

So far, extensive studies have been focused on improving the photocatalysis of dyes by magnetic and quantum dot hybrids. Hybrid nanoparticles of $NiFe_2O_4$/ZnO have been prepared by various methods including solvothermal process, simple hydrothermal process, combustion synthesis, and ultrasonic techniques for decolorization [26,27].

Due to the promising photocatalytic behavior of $NiFe_2O_4$/ZnO, this magnetic nanocomposite was synthesized by numerous researchers including Rahmayeni *et al.* [21], Adeleke *et al.* [9], and Hua-Yue Zhu *et al.* [15].

In comparison to other photocatalysts, it seems that photodegradation of Coomassie blue G-250 by $NiFe_2O_4$/ZnO nanocomposites decreases in the presence of La- and Ce-doped ZnO. Moreover, the absorption intensity declines with increase in irradiation time. On the other hand, no observable degradation of the dye could be seen under visible light in the absence of doped photocatalysts [28]. In the presence of La- and Mo-doped TiO_2, the absorption intensity decreases with increase in irradiation [29]. Despite an increase in the absorption intensity with enhanced irradiation time in $NiFe_2O_4$/ZnO nanocomposites, more effective dye degradation occurs in a short time due to the formation of a heterogeneous bond between ZnO and $NiFe_2O_4$ nanoparticles. Furthermore, compared to commercial P25, $NiFe_2O_4$/ZnO nanocomposites have superior photodegradation. Studies have shown that commercial P25 only manages to degrade a small fraction of the dyes, while magnetic catalysts degrade dyes to a higher percentage [30]. As is known, coupling ZnO and magnetic nanoparticles results in a semiconductor photocatalyst with improved activity. Therefore, magnetic nanoparticles/ZnO can be a useful alternative to commercial P25. Owing to the remarkable magnetic properties of ferrites, photocatalyst recovery and reuse are also possible [30].

In this research, the $NiFe_2O_4$/ZnO nanocomposite was prepared by solidification and calcination methods in all steps even for the preparation of ZnO and nickel ferrite magnetic particles. The nanoparticles were characterized by X-ray diffraction (XRD), scanning electron microscopy, vibrating sample magnetometry (VSM), and Fourier transform infrared (FTIR) techniques. The photocatalytic degradation of Coomassie blue G-250 pigments was also studied under visible and UV radiation using $NiFe_2O_4$, ZnO, and $NiFe_2O_4$/ZnO to examine the benefit of the $NiFe_2O_4$/ZnO nanocomposite, which has not been investigated before. Furthermore, $NiFe_2O_4$/ZnO can serve as an excellent nanocomposite for the degradation of the dye. However, the effect of various parameters such as pH, contents of catalysts, and duration of dye degradation has not been studied in the

photocatalytic degradation of the Coomassie blue G-250 pigment. Moreover, despite extensive studies on the photodegradation of Coomassie blue G-250 using different photocatalysts, the $NiFe_2O_4$/ZnO nanocomposite has not yet been investigated.

2. Materials and methods

2.1. *Materials*

For synthesis, the starting chemical materials used in this work are $Ni(NO_3)_2 \cdot 6H_2O$, $Fe(NO_3)_3 \cdot 9H_2O$, $Zn(NO_3)_2 \cdot 6H_2O$, NaOH, ethanol, citric acid, oxalic acid, and thiourea (all materials were purchased from Merck). All reagents are analytically pure and are used without further purification.

2.2. *Synthesis of $NiFe_2O_4$ magnetic nanoparticles*

To prepare nickel ferrite nanoparticles, 9.31 g nickel nitrate was dissolved together with 20.17 g citric acid and 25.86 g iron nitrate in 150 mL of distilled water in a large beaker by using a magnetic stirrer for 1 h. After complete dissolution, it was subjected to magnetic motion at a temperature of 80 °C for 2 h. Then the pre-prepared (ammonia:water) solution was added dropwise using a decanter until a pH value of 7 was reached. After the addition of the ammonia solution, the heater temperature was adjusted to 180 °C until the solution turned into a dark gel. The gel began to diminish and dry after the motion was continued. When powder particles erupted from the surface, heating was stopped. The whole gel converted to ash was milled by a mortar, and the resulting soft powder was calcined to remove the impurities at 1000 °C for 1 h.

2.3. *Synthesis of ZnO*

At this stage, 2.97 g $Zn(NO_3)_2 \cdot 6H_2O$ was dissolved in 50 mL ethanol by a magnetic stirrer for ZnO synthesis. Separately, 1.26 g oxalic acid was dissolved in 50 mL ethanol by a magnetic stirrer. These two solutions were mixed after complete dissolution by a magnetic stirrer; thus, a white gel with pH 5 was obtained. It was kept for 19 h at room temperature to complete the reaction. Then, it was dried in a vacuum oven at a temperature of 60 °C. A white powder was

produced, which was milled with a mortar and calcined at 400 °C for 4 h. After calcination, the resulting precipitate was rinsed several times with distilled water and acetone to remove contaminants and was dried at room temperature.

2.4. *Synthesis of $NiFe_2O_4$/ZnO nanocomposite*

One gram thiourea was completely mixed with 2 g ZnO and 0.1 g nickel ferrite magnetic nanoparticles and calcined for 8 h at 800 °C. This ultimately resulted in a $NiFe_2O_4$/ZnO nanocomposite. Figure 1 schematically shows the synthesis of the $NiFe_2O_4$/ZnO nanocomposite from nickel ferrite and ZnO.

2.5. *Characterization*

The XRD analysis of the samples was conducted by using STOE STADI-P with Cu Kα radiation (λ = 1.54060 Å) at a scanning rate of 0.02°/s and a 2θ range of 20–80° at room temperature. Field emission scanning electron microscopy (FESEM) was applied to investigate the synthesized samples. The FTIR spectroscopy data were recorded in the spectral range of 400–4000 cm^{-1} using a Nexus 870 spectrometer. Photocatalytic properties of the nanocomposite were evaluated by ultraviolet–visible spectroscopy using a UV-1700 spectrophotometer. The magnetic properties of the $NiFe_2O_4$/ZnO nanocomposite and $NiFe_2O_4$ nanoparticles were measured at room temperature by a Quantum Design MPMS-XL-7 superconducting quantum interference device whose external magnetic field ranges from −15 kOe to +15 kOe.

2.6. *Photocatalytic activity test*

The photocatalytic activity of the synthesized $NiFe_2O_4$, ZnO, and $NiFe_2O_4$/ZnO was studied by measuring the degradation of the Coomassie blue G-250 dye solution. For each experiment, 0.025, 0.050, 0.075, and 0.1 g of samples were dispersed in 25 mL of the dye solution (8 ppm) in a hot water bath (30 °C) under visible light from an incandescent lamp (200 W, 238.66 cd) and UV light and then investigated for 1 h. Two milliliters of samples were collected after irradiation (in 10 min intervals) and centrifuged at
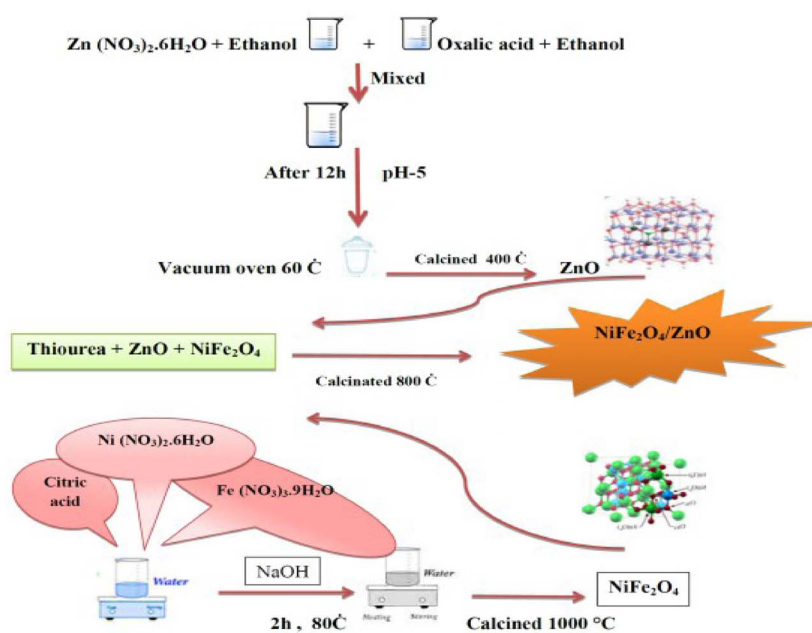
Figure 1. Schematic diagram: synthesis of $NiFe_2O_4$/ZnO nanocomposite.

10,000 rpm for 5 min. The supernatants were monitored by measuring their absorption by spectrophotometry at a wavelength of 553 nm. After checking different sample ($NiFe_2O_4$, ZnO, and $NiFe_2O_4$/ZnO) contents, the optimal content was used to examine the dye degradation at various pH values (9, 7, and 3) with the same procedure being performed on ZnO and $NiFe_2O_4$ but for a different time period. The percentage of dye degradation was calculated according to (1).

$$\text{Degradation}(\%) = (A_0 - A)/A_0 \times 100, \qquad (1)$$

where A_0 is the initial concentration of Coomassie blue G-250 and A is the concentration of Coomassie blue G-250 after t minutes.

3. Results and discussion

3.1. *Powder X-ray diffraction analysis*

Figure 2 shows the XRD patterns of nickel ferrite, ZnO, and $NiFe_2O_4$/ZnO nanocomposite. The sample diffraction peaks at 2θ values of 31.64°, 34.45°, 36.30°, 47.57°, 56.57°, 63.68°, 67.91°, and 69.04° were indexed as (100), (002), (101), (102), (110), (103),
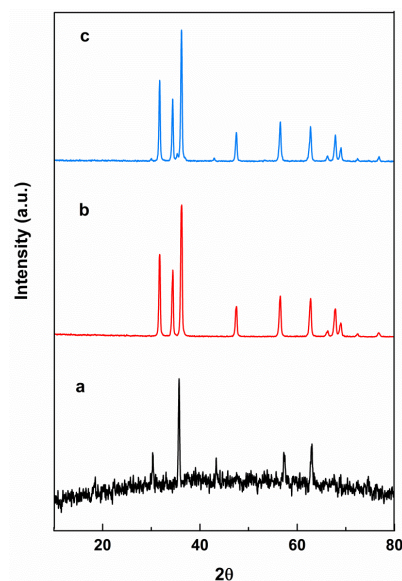

Figure 2. XRD patterns of (a) $NiFe_2O_4$, (b) ZnO, and (c) $NiFe_2O_4$/ZnO.

(112), and (201) planes, respectively, corresponding to the ZnO hexagonal crystal (JCPDS card no. 00-036-1451). The XRD pattern with 2θ values of 30.31°,
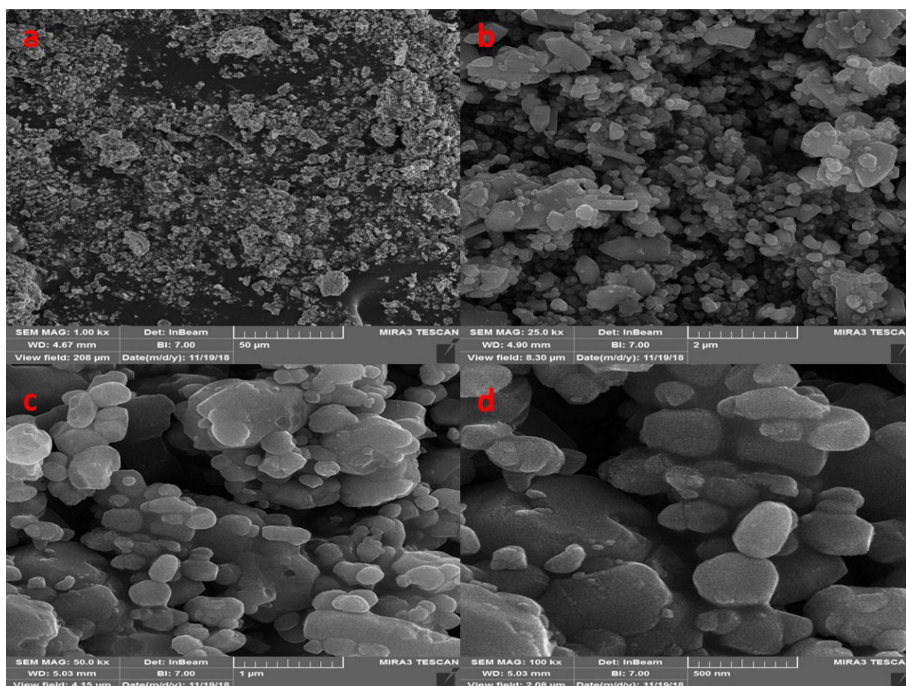
Figure 3. FESEM images of (a) NiFe$_2$O$_4$, (b) ZnO, and (c, d) NiFe$_2$O$_4$/ZnO nanocomposite.

35.71°, 43.32°, 57.24°, and 62.98° could be indexed to (220), (311), (410), (511), and (440) planes, respectively, confirming the presence of the nickel ferrite cubic structure (JCPDS card no. 01-074-2081). The nanocomposite pattern exhibited peaks of ZnO and NiFe$_2$O$_4$. Peaks of (100), (002), (101), (102), (110), (103), (112), and (201) belong to the hexagonal phase of ZnO, while small peaks of (220), (311), and (410) are associated with the nickel ferrite spinel phase. Comparatively, no visible impurity peaks were observed. A weak peak in NiFe$_2$O$_4$ at 2θ = 57.24° (511) disappeared in NiFe$_2$O$_4$/ZnO hybrids. This is in good agreement with the results by Hua-Yue Zhu *et al.* [15]. The average sizes of NiFe$_2$O$_4$, ZnO, and NiFe$_2$O$_4$/ZnO nanoparticles were 46.2, 58.2, and 49 nm, respectively, according to the Debye–Scherrer equation (2).

$$D = k\lambda/\beta\cos\theta, \qquad (2)$$

where D denotes the crystalline size, β is the full-width at half-maximum, K is the shape factor, θ represents the Bragg angle corresponding to the peak, and λ is the wavelength of X-rays.

3.2. *Morphology of nanoparticles*

The morphology of nanoparticles was analyzed by FESEM. All images are shown in Figure 3. The FESEM image of ZnO shows the structure of hexagonal nanoparticles with a size of 48–52 nm. The FESEM image of nickel ferrite nanoparticles shows a cubic structure with a size of 25–31 nm and the NiFe$_2$O$_4$/ZnO nanocomposite image shows different densities and morphologies. The reason for the difference in density is due to magnetic absorption between nickel ferrite and zinc oxide.

3.3. *Analysis of magnetic properties*

Figure 4 plots the VSM of nanoparticles, nickel ferrite, and the NiFe$_2$O$_4$/ZnO nanocomposite. The saturated magnetism of nickel ferrite nanoparticles alone (49.86 emu/g) is higher than that in saturated nanocomposites (3.09 emu/g). ZnO is well identified as a diamagnetic material, while the synthesized nickel ferrite nanoparticles are ferromagnetic. Paramagnetic properties in nanocomposites are due to ferromagnetic nickel ferrite bonding to diamagnetic
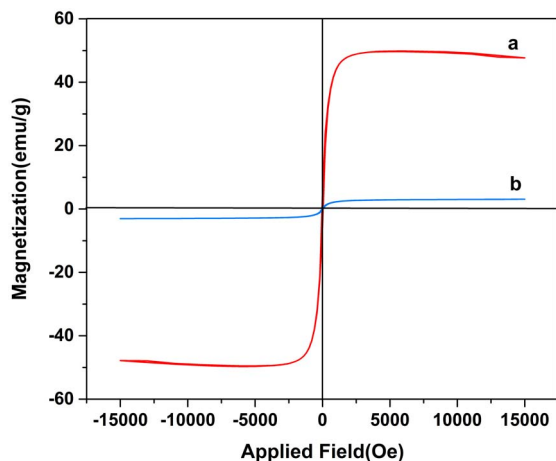
Figure 4. Vibrating sample magnetometer curves of (a) $NiFe_2O_4$ and (b) $NiFe_2O_4/ZnO$ nanocomposite.

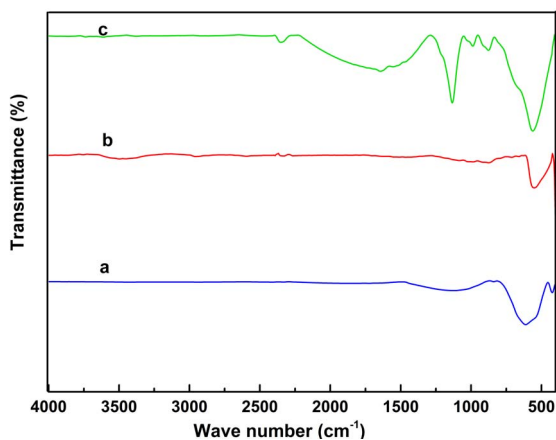**Figure 5.** FTIR spectral curve of (a) $NiFe_2O_4$, (b) ZnO, and (c) $NiFe_2O_4/$ ZnO.

ZnO. The magnetic properties of the nanocomposite facilitate the process of separating the catalyst from the liquid.

3.4. *FTIR analysis*

The interaction of nickel ferrite and zinc oxide in the nanocomposite was investigated using the FTIR spectrum. This is shown in Figure 5. The peak in the spectrum of the nanocomposite at 562 cm^{-1} is associated with ZnO stretching vibration or a combination of ZnO and ferrite. Peaks at 876–987 cm^{-1} are at-

tributed to the section of 1, 3 metallic aromatic rings. The peaks at 1133–1644 cm^{-1} are indicative of the OH at the surface and the bands outside the surface. The negligible peak at 2351 cm^{-1} could be attributed to atmospheric CO_2. In the case of nickel ferrite, the peaks at 424–440 cm^{-1} and 580–600 cm^{-1} are attributed to the stretching vibration of the oxygen–metal (Fe^{3+}–O^{2-}) bond in tetrahedral and octahedral sites, respectively. The peak in the 1055–1130 cm^{-1} region is related to OH bending vibration. The results are in good agreement with those obtained by Adeleke *et al.* [9].

4. Photocatalytic activity

The photocatalytic activity of $NiFe_2O_4$, ZnO, and $NiFe_2O_4/ZnO$ was evaluated by the degradation of Coomassie blue G-250 dye under visible light from an incandescent lamp and UV light. As observed in Figure 6(a), when different contents of samples were exposed to UV light, in the presence of $NiFe_2O_4$, the degradation percentage of Coomassie blue G-250 was 15.5%. This shows no significant increase in the Coomassie blue G-250 degradation. Pure ZnO exhibited 40.01% Coomassie blue G-250 degradation. However, the degradation of Coomassie blue G-250 was rapidly increased on addition of $NiFe_2O_4/ZnO$ nanocomposite (86.15%). The results indicated that the photocatalytic activity of $NiFe_2O_4/ZnO$ nanocomposites is higher than that of pure ZnO and $NiFe_2O_4$. Moreover, by increasing the photocatalyst content, the Coomassie blue G-250 degradation percentage increased for 1 h. Besides, the results of the photocatalytic activity of different contents of samples under visible light from incandescent lamps (Figure 6(b)) were similar to those of UV light but with a lesser degradation percentage of the Coomassie blue G-250 dye. These results indicated that the photocatalytic activity of the composite was improved due to the formation of a heterogeneous bond among ZnO, $NiFe_2O_4$, and the $NiFe_2O_4/ZnO$ nanocomposite. This enabled the composite to serve as a good photoactive agent under both UV and visible light.

4.1. *Investigation of pH*

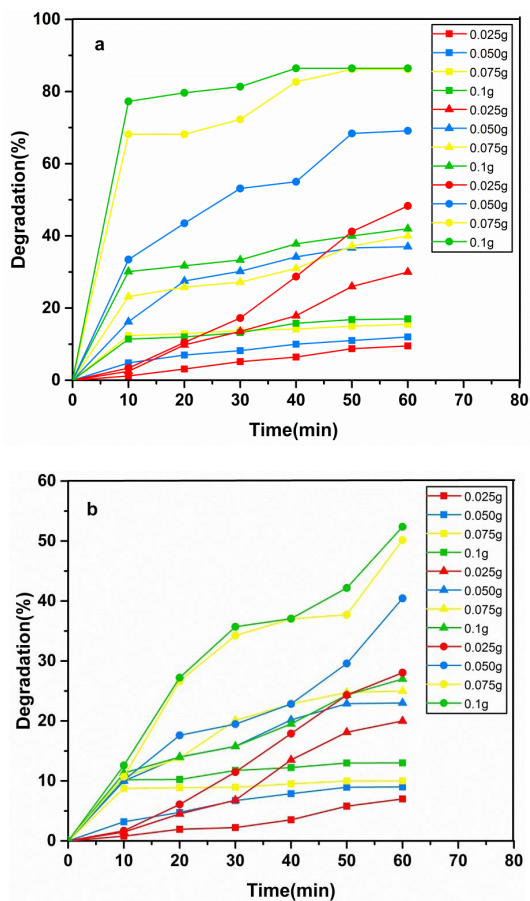The role of pH in dye degradation by $NiFe_2O_4$, ZnO, and $NiFe_2O_4/ZnO$ was also studied. NaOH 0.1 M

Figure 6. The degradation percentage of Coomassie blue G-250 for various amounts of ■ NiFe$_2$O$_4$, ▲ ZnO, and • NiFe$_2$O$_4$/ZnO under (a) UV light and (b) visible light.

Figure 7. The degradation percentage of Coomassie blue G-250 dye for various pH values of ■ NiFe$_2$O$_4$, ▲ ZnO, and • NiFe$_2$O$_4$/ZnO under (a) UV light irradiation and (b) visible light irradiation.

and HCl 0.1 M were used to adjust pH and evaluate the photocatalytic behavior in three environments: acidic, neutral, and alkaline. The results of the sampling at different time intervals under UV light (Figure 7(a)) demonstrate that the degradation percentage of Coomassie blue G-250 was more effective in acidic media (pH 3) for all samples. The degradation efficiency declined with increase in pH. This can be due to the ionic form of Coomassie blue G-250 in the acidic medium with positive surface charges and hence electrostatic interactions in the acidic environment as compared with the alkaline environment in which the dye is in anionic form and is negatively charged. Therefore, in contrast to most organic dyes, the studied dye exhibited better degradation
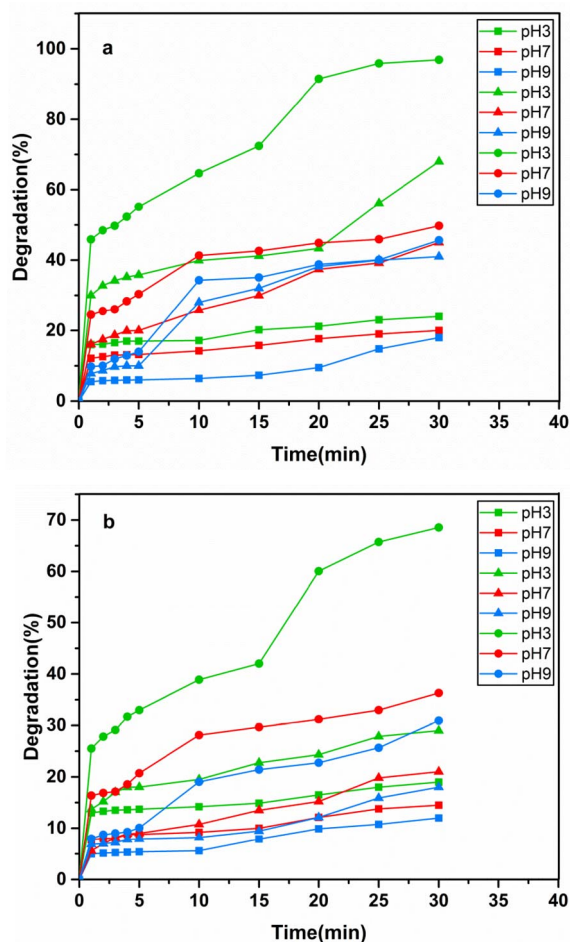
in acidic environments. Moreover, in the presence of NiFe$_2$O$_4$, the degradation percentage of Coomassie blue G-250 was 24%, showing no significant increase compared to that of pure ZnO (68%). However, in the case of the NiFe$_2$O$_4$/ZnO nanocomposite, the degradation of Coomassie blue G-250 showed a rapid increase to 96.90%. By decreasing the pH and by the combination of NiFe$_2$O$_4$ with ZnO, the degradation performance was improved. Additionally, the photocatalytic activity of the samples was investigated at the optimal photocatalyst content (0.075 g) under a similar condition but by using visible light from an
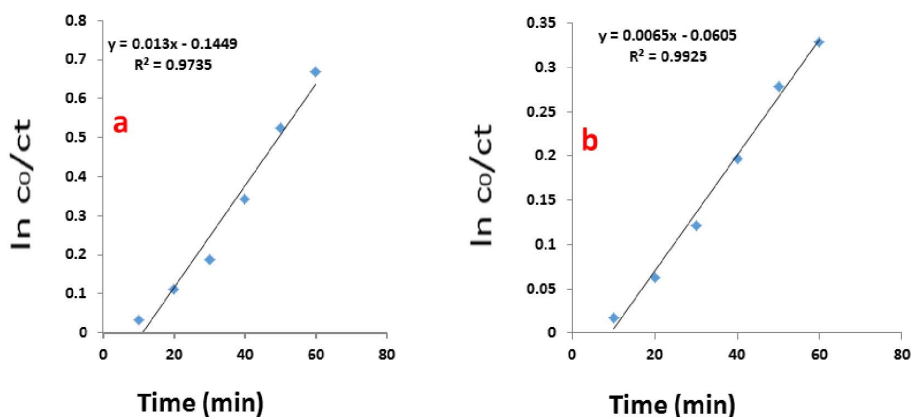
Figure 8. Plot (Ln C_0/C) for degradation of Coomassie blue G-250 using $NiFe_2O_4/ZnO$ as the catalyst under (a) UV light and (b) visible light.

incandescent lamp. From Figure 7(b), it can be observed that the dye degradation of samples was similar to that under UV light as degradation was enhanced with decreasing pH. As observed, the highest Coomassie blue G-250 degradation occurred in the acidic environment (pH 3) due to the ionic form of the dye and its electrostatic interactions with the acidic environment. By increasing the pH, the organic photosynthetic degradation rate of the organic dye was slowly decreased. This trend can be attributed to the pH-dependent electrostatic interactions between the dye and the photocatalyst. The kinetics of the photocatalytic reaction were also assessed under visible and UV radiation as presented in Figure 8(a, b). The effect of initial dye concentration on the photocatalytic degradation rate for the abovementioned cases can be described by the first-order kinetic model. The constant rate for each photocatalyst was calculated according to Langmuir's relation (3).

$$\ln C_0/C = k \times t, \qquad (3)$$

where C_0 is the initial dye concentration, C is the secondary concentration at time t, and k is the constant rate. The correlation constant for the UV light was calculated as $R^2 = 0.9735$ and that for the visible light was calculated as $R^2 = 0.9925$.

5. Conclusions

In this research, ZnO and magnetic nickel ferrite nanoparticles were prepared by solidification and calcination methods. Then, the nanocomposite was synthesized by a simple solid-state method. It should be noted that calcination was used in all stages of the synthesis for both nanoparticles and nanocomposites. The size of the nanoparticles was smaller than 50 nm. Microstructural studies indicated that the prepared nanocomposite included spinel nickel ferrite magnetic particles and ZnO. Regarding the magnetic saturation of the ferromagnetic nickel ferrite and superparamagnetic behavior of the nanocomposite, they can be easily recovered through magnetic force. The photocatalytic activity of the samples ($NiFe_2O_4$, ZnO, and $NiFe_2O_4/ZnO$) was studied using Coomassie blue G-250 dye at different contents and pH values under visible and UV light. The results showed that combining $NiFe_2O_4$ and ZnO enhances the photocatalytic effect. Although the photocatalytic activity was better under UV light, remarkable dye degradation was observed under visible light as well.

References

[1] S. Yi Lee, S. Jin Park, *J. Ind. Eng. Chem.*, 2013, **19**, 1761-1769.

[2] K. Pamecha, V. Mehta, B. V. Kabra, *Adv. Appl. Sci. Res.*, 2016, **7**, 95-101.

[3] D. R. Shinde, P. S. Tambade, M. G. Chaskar, K. M. Gadave, *Drink. Water Eng. Sci*, 2017, **10**, 109-117.

[4] B. Yang, Y. Gao, D. Yan, H. Xu, J. Wang, *Int. J. Environ. Res. Public Health Article*, 2018, **15**, 1523.

[5] B. Legube, N. Leitner, *Catalysis. Today*, 1999, **53**, 61-72.

[6] Z. K. xin1, W. H. wei1, X. S. guang, *J. Environ. Prot. Sci.*, 2007, **1**, 52-61.

[7] D. R. Simpson, *Water Res.*, 2008, **42**, 2839-2848.

[8] V. Jadhav, P. Chikode, G. Nikam, S. Sabale, *Mater. Today: Proc.*, 2016, **3**, 4121-4127.

[9] J. T. Adelekea, T. Theivasanthib, M. Thiruppathib, M. Swaminathanb, T. Akomolafec, A. B. Alabi, *Appl. Surface. Sci.*, 2018, **455**, 195-200.

[10] J. Z. Konga, A. D. Lia, H. F. Zhaia, H. Lia, Q. Y. Yanb, J. Mab, D. Wua, *J. Hazards Mater.*, 2009, **171**, 918-923.

[11] V. Sanna, N. Pala, V. Alzari, D. Nuvoli, M. Carcelli, *Mater. Lett.*, 2016, **162**, 257-260.

[12] E. Ferdosia, H. Bahiraeia, D. Ghanbarib, *Separation Purification Technol.*, 2019, **211**, 35-39.

[13] I. Kazeminezhad, A. Sadollahkhani, M. Farbod, *Mater. Lett.*, 2013, **92**, 29-32.

[14] K. M. Parida, N. Sahu, N. R. Biswal, B. Naik, A. C. Pradhan, *J. Colloid Interface Sci.*, 2008, **318**, 231-237.

[15] H. Y. Zhu, R. Jiang, Y. Q. Fu, R. R. Li, J. Yao, S. T. Jiang, *Appl. Surf. Sci.*, 2016, **369**, 1-10.

[16] N. Jamarun, S. Arief, *Orient. J. Chem.*, 2016, **32**, 1411-1419.

[17] C. Xu, L. Cao, G. Su, W. Liu, H. Liu, Y. Yu, X. Qu, *J. Hazards Mat.*, 2010, **176**, 807-813.

[18] N. R. Su, P. Lv, M. Li, X. Zhang, M. Li, J. Niu, *Mater. Lett.*, 2014, **122**, 201-204.

[19] T. J. Castro, S. W. Da Silva, F. Nakagomi, N. S. Moura, J. Franco, P. C. Morais, *J. Magn. Magn. Mater.*, 2015, **389**, 27-33.

[20] S. Sunitha, A. Nageswararao, J. Karthikeyan, *Orient. J. Chem.*, 2015, **31**, 107-112.

[21] Rahmayeni, Zulhadjri, N. Jamarun, Emriadi, S. Arief, *Orient. J. Chem.*, 2016, **32**, 1411-1419.

[22] Rahmayeni, S. Arief, Y. Stiadi, R. Rizal, Zulhadjri, *Indo. J. Chem.*, 2012, **12**, 229-234.

[23] E. Casbeer, V. K. Sharma, X. Z. Li, *Separation Purification Technol.*, 2012, **87**, 1-14.

[24] A. Ren, C. Liu, Y. Hong, W. Shi, S. Lin, P. Li, *Chem. Eng. J.*, 2014, **258**, 301-308.

[25] R. S. Melo, F. C. Silva, K. R. M. Moura, A. S. De Menezes, F. S. M. Sinfrônio, *J. Magn. Magn. Mater.*, 2015, **381**, 109-115.

[26] J. Jiang, L. H. Ai, L. C. Li, H. Liu, *J. Alloys Comp.*, 2009, **484**, 69-72, Contents.

[27] H. Zhu, R. Jiang, Y. Fu, R. Li, J. Yao, *Appl. Surf. Sci.*, 2016, **369**, 1-10.

[28] W. Raza, M. Haque, M. Muneer, *Appl. Surf. Sci.*, 2014, **322**, 215-224.

[29] M. Haque, W. Raza, M. Muneer, M. Fleisch, A. Hakki, D. Bahnemann, *J. Alloys Compd.*, 2015, **632**, 837-844.

[30] R. Ciocarlan, E. Seftel, R. Gavrila, M. Suchea, M. Batuk, M. Mertens, J. Hadermann, P. Cool, *J. Alloys Compd.*, 2020, **820**, 12-14.